



Label-Free Protein Analysis by Pyro-Electrohydrodynamic Jet Printing of Gold Nanoparticles

Veronica Vespini¹, Simonetta Grilli¹, Pietro Ferraro^{1*}, Romina Rega¹, Heidi Ottevaere², Yunfeng Nie², Pellegrino Musto^{3*} and Marianna Pannico³

¹National Research Council of Italy (CNR-ISASI), Institute of Applied Sciences and Intelligent Systems, Pozzuoli, Italy, ²Vrije University of Brussels Pleinlaan, Brussels, Belgium, ³Composites and Biomaterials, National Research Council of Italy (CNR-IPCB), Institute for Polymers, Pozzuoli, Italy

OPEN ACCESS

Edited by:

Carlo Altucci,
University of Naples Federico II, Italy

Reviewed by:

Fulvia Villani,
National Agency for New
Technologies Energy and Sustainable
Economic Development,
United Kingdom
Claudio Parolo,
Instituto Salud Global Barcelona
(ISGlobal), Spain

*Correspondence:

Pietro Ferraro
pietro.ferraro@cnr.it
Pellegrino Musto
pellegrino.musto@cnr.it

Specialty section:

This article was submitted to
Nanobiotechnology,
a section of the journal
Frontiers in Bioengineering and
Biotechnology

Received: 18 November 2021

Accepted: 24 January 2022

Published: 22 February 2022

Citation:

Vespini V, Grilli S, Ferraro P, Rega R,
Ottevaere H, Nie Y, Musto P and
Pannico M (2022) Label-Free Protein
Analysis by Pyro-Electrohydrodynamic
Jet Printing of Gold Nanoparticles.
Front. Bioeng. Biotechnol. 10:817736.
doi: 10.3389/fbioe.2022.817736

The pyro-electrohydrodynamic jet (p-jet) printing technology has been used for the fabrication of confined assemblies of gold nanoparticles with a round shape and a diameter ranging between 100 and 200 μm . The surface-enhanced Raman spectroscopy (SERS) performance of the p-jet substrate was evaluated by using Rhodamine 6G (R6G) as a reference. The results demonstrate that this kind of SERS substrate exhibits strong plasmonic effects and a significant reproducibility of the signal with a coefficient of variation below 15%. We tested the signal behavior also in case of the bovine serum albumin (BSA) as a model analyte, to demonstrate the affinity with biomolecules. Strong SERS activity was measured also for BSA across the whole spot area. The spectral patterns collected in different locations of the sensing area were highly reproducible. This observation was substantiated by multivariate analysis of the imaging datasets and opens the route towards a potential application of this kind of SERS substrate in biosensing.

Keywords: SERS spectroscopy, sensors, jet printing, colloids, plasmonic

1 INTRODUCTION

Surface-enhanced Raman spectroscopy (SERS) is a versatile analytical technique widely used for molecular detection and for the investigation of a great variety of chemical and biological samples (Aroca, 2006; Le Ru and Etchegoin, 2008). Among the numerous advantages of this technique are the excellent sensitivity, the fingerprint character of the spectrum, which allows identification and multiplex analysis, and the sampling flexibility (from macro to submicro measurements, remote sampling *via* fiber optics) (Schlucker, 2011). In real-world applications, the major drawback is related to the non-uniform response of 2D SERS sensors, i.e., those obtained by deposition of colloidal solutions onto suitable substrates (Schlucker, 2011; Fornasaro et al., 2020). The effect is due to the inhomogeneous distribution of the nanoparticles across the sensing surface, which generally results after drying. Attempts to alleviate this issue mostly involve the chemical modification (derivatization) of the substrate surface, but so far, limited success has been achieved (Wang and Kong, 2015; Fornasaro et al., 2020). The problem is particularly relevant in quantitative analysis where spatial and temporal consistency of the signal is mandatory (Fornasaro et al., 2020). Strictly related to the non-uniform SERS activity of 2D sensors is the undersampling problem (Shin and Chung, 2013): in most experimental setups, spectral collection is made through a microscope objective, which irradiates (and collects signals from) an area of up to 200 μm in diameter. Thus, the

spectrum is poorly representative of the whole sample (dropping produces footprints between 0.5 and 5.0 mm in diameter), and the SERS signals display a large spatial variability. To minimize this problem, several strategies have been proposed, each with its own disadvantages: 1) collecting and averaging spectra at many different points, which is a lengthy and cumbersome procedure, unsuitable for high-throughput analyses; 2) rotation of the sample during spectral collection, which requires specialized accessories and produces low-quality spectra; and 3) simultaneous wide-area illumination (WAI), also requiring specific setups and mainly used in the single-frequency collection mode (McGoverin et al., 2008; Strachan et al., 2010; Shin and Chung, 2013). We propose an alternative approach to the undersampling problem consisting in the fabrication of a sensing area whose shape and dimensions conform to those of the laser spot, thus allowing the whole deposition to be sampled in a single acquisition (Pannico et al., 2020). The confinement of the plasmonic nanostructure within an area of precisely controlled size and shape provides the additional advantage of increasing the nanoparticle density, which enhances the SERS sensitivity. The micro-confinement of plasmonic nanoobjects has been approached in several ways, among which are electrospinning (Zhang et al., 2012), self-assembly (García-Lojo et al., 2019; Lin et al., 2019), and electro-deposition combined with lithography (Lee et al., 2019).

Recently, inkjet printing has been developed into an effective method for fabricating micro-/nanostructure arrays as this type of printing can simply drop the ink solution in a fixed volume onto a set position (Lee et al., 2005; Yakovlev et al., 2016). Both Ag and Au nanoparticles have been printed on cellulose paper or silicon wafers for SERS purposes (Yu and White, 2010; Yang et al., 2015). Even though inkjet printing exhibits advantages in terms of controllability, still challenges remain in terms of nozzle clogging with consequent requirements of ink mixing solutions for changing sample viscosity and/or surface tension.

Here, we present an innovative SERS substrate achieved through the p-jet printing technique. In particular, we propose a significant step forward compared to the proof-of-concept published in Pannico et al. (2020) with a top-down jetting modality and with a micro-engineered loading support. This configuration produces a stable meniscus profile independent from the load volume, allowing us to obtain spots of gold nanoparticles with high reproducibility in terms of both size and SERS signal, thus significantly increasing the statistical validity of this innovative SERS substrate.

The p-jet printing is an attractive technology for fabricating micro-scale patterns due to its advantages in terms of low cost, efficient use of materials, and waste reduction (Ferraro et al., 2010). By precisely controlling the printing droplets, one can print high-resolution patterns with versatile materials directly on substrate thanks to an electric field generated by the pyroelectric effect from lithium niobate (LN) crystal subjected to a temperature gradient. Additionally, the p-jet allows us to print the colloidal solution of nanoparticles through a non-contact modality avoiding nozzles and external electrodes, thus overcoming the clogging-related issues and the need for mixing buffers (Nie and Kumacheva, 2008).

We characterize here the SERS signal of round-shaped spots, with a diameter in the range of 150–200 μm , made of an assembly of gold nanoparticles, first with R6G and then with a typical test protein, BSA. In fact, the detection of proteins in complex mixtures, with or without preliminary separation, is a central problem in biochemical research (Bergveld, 1991; Westermeier and Marouga, 2005; Han et al., 2009) (Mann et al., 2001; Domon and Aebersold, 2006) (Ladokhin, 2006; Hillger et al., 2007), and SERS spectroscopy is the object of interest for this kind of application (Han et al., 2008; Han et al., 2009; Foti et al., 2018). When the measurement is carried out in colloidal solutions, the sensitivity is lowered by dilution and the spectrum shows a spatial variability, possibly reflecting multiple binding sites and/or conformational rearrangements around the binding site (Szekeres and Kneipp, 2018; Kuhar et al., 2021). The inconsistency of the SERS pattern complicates the use of the method for identification and quantification purposes. We demonstrate here how this innovative SERS substrate displays a substantial SERS activity and, above all, a good reproducibility of the spectrum across the whole sensing area, as confirmed by multivariate analysis of the hyperspectral data sets. These features open the perspective of multiplex analysis and quali/quantitative assays in complex biological mixtures.

2 MATERIALS AND METHODS

2.1 Materials

Trisodium citrate (TC), gold (III) chloride trihydrate ($\text{HAuCl}_4 \cdot 3\text{H}_2\text{O}$), ascorbic acid (AA), sodium borohydride (NaBH_4), cetyltrimethylammonium bromide (CTAB), rhodamine 6G (R6G), and bovine serum albumin (BSA) have been supplied by Sigma Aldrich (Italy) and used as received. Milli-Q water was used for the preparation of gold nanoparticles. LN, a rhombohedral crystal belonging to the point group 3 m, was bought from Crystal Technology Inc. in the form of both sides polished, 500 μm thick, z-cut, and 3-inch diameter. The wafer was cut into square samples $2 \times 2 \text{ cm}^2$ in size by a standard diamond saw. The deposition slide was a coverslip, bought from Sigma Aldrich, consisting of an untreated glass substrate $24 \times 60 \text{ mm}$ in size and 0.2 mm thick.

2.2 Fabrication of the P-jet SERS Substrate

Gold nanoparticles (AuNPs) were synthesized in aqueous solution by using the seed-mediated growth method as described in a previous work (Pannico et al., 2020). A SERS substrate was obtained by deposition of the colloidal solution on a glass substrate by pyro-electrohydrodynamic jet-printing technique.

2.2.1 Pyroelectric Effect

The spontaneous polarization P_s of the LN crystal changes according to $\Delta P_s = p \Delta T$, where p is the pyroelectric coefficient and ΔT is the temperature variation ($p = -8.3 \times 10^{-5} \text{ C m}^{-2} \text{ K}^{-1}$ at $T = 298 \text{ K}$). At thermal equilibrium, the spontaneous polarization of the crystal is completely screened by the external charges accumulated on the crystal surfaces, and

no electric field is present. When the crystal is stimulated through a temperature variation, an uncompensated surface charge density $= \Delta P_s$ and electric potential difference $\Delta U \sim \frac{\Delta P_s d}{\epsilon_0 \epsilon}$ appear on the crystal surfaces (here, d is crystal thickness and ϵ_0 and ϵ are dielectric constants of vacuum and of the crystal, respectively). This potential difference can reach 10^4 V for millimeter-sized crystal thickness and ΔT of about 10 K.

2.2.2 Thermal Stimulation

The thermal stimulation is insured using a tungsten wire-based heater onto lower side of the LN crystal, able to apply a temperature gradient on LN and to generate the pyroelectric effect. The heat transfer device has been fabricated in lab workshop with a tungsten wire having 300 μm diameter and a pointed shape. The heater is powered by a high-current power supply that is modulated with a 5-V transistor-transistor logic (TTL) signal generated by a conventional signal generator. The “ON time” represents the time lapse in which heating current passes through the heater, “Total time” is the period of thermal stimulus, and “OFF time” = “Total time” – “ON time” is the time during which the pyroelectric layer comes into thermal equilibrium with the environment. The electrical circuit is set by enabling the power supply (Lab. Grade Switching Mode Power Supply HCS-3300), and a waveform generator (33220A Function/Arbitrary Waveform Generator, 20 MHz) is utilized to set a step function with assigned on and off times. In addition, the system includes a fan blowing air to the cooling structure of pyroelectric stage, LiNbO₃ crystal. The aim of the efficient cooling is to enable faster heating cycles for the dispensing. The electrical and thermal characteristics of the investigated heater is presented in a table, where R , I_{ON} , P_{ON} , T_{ON} , and P_{MEAN} are heater resistance, heating pulse current, heating pulse power, heating pulse temperature, and mean power of periodic heating pulses, respectively, as shown in **Table 1**.

2.2.3 Loading Support Configuration

Loading support is made of a micro-orifice in PMMA HESAglass using a hot molding approach; the upper diameter is around 5 mm while the bottom orifice is around 1 mm. A mother drop (around 10 μl) of sample is loaded manually by a standard pipette into the engineered micro-orifice of the loading support, and a stable liquid meniscus emerged on the opposite side. The aim is to achieve a liquid meniscus and, consequently, a more accumulated charge on its apex to shorten the diameter of the ejected droplet and improve its repeatability. The surface smoothness has been also measured to be within the sub-micron range, demonstrating a good smoothness of the orifice. This allows to have an innovative contact-free modality as a means for generating a pointed meniscus exposed to the pyro-electric field for tiny-droplet ejection by p-jet. In addition, the system with orifice translates the loading layer in Z direction with a manual translation stage.

2.3 SERS Activity

The SERS performance was evaluated by using R6G as a reference. The p-jet SERS substrate was washed several times with Milli-Q water, dried under nitrogen flux, and then

functionalized with a 100 μM water solution of R6G: 30 L of R6G solution were dropped on the substrate to fully cover the whole spots. The substrate was kept at room temperature, for a sufficient time, to allow water evaporation. Before Raman characterization, the substrate was washed again with water to remove the excess of unreacted R6G and dried under nitrogen flux. The same procedure was adopted when testing the present analytical platform for BSA detection. Thus, a 100-M water solution of BSA was deposited by drop-casting. The substrate was washed with Milli-Q water several times to remove the excess protein and dried under nitrogen flux.

2.4 Techniques

2.4.1 Transmission Electron Microscopy

The AuNP shape and average diameter were estimated by bright-field transmission electron microscopy (TEM) performed on an FEI Tecnai G12 Spirit Twin (LaB6 source) equipped with an FEI Eagle 4K CCD camera (Eindhoven, The Netherlands) operating with an acceleration voltage of 120 kV. Samples for TEM examination were prepared by immersing a carbon-coated copper grid in the colloidal solution, followed by drying. TEM images were acquired in different sample areas and were transferred to the MATLAB computational platform (MathWorks, Natick, MA, United States) for further processing. Statistical image analysis (SIA) was performed by the PLS/MIA toolbox (Eigenvector Research Inc. Manson, WA, United States), running under the MATLAB environment.

2.4.2 Zeta Potential Measurements

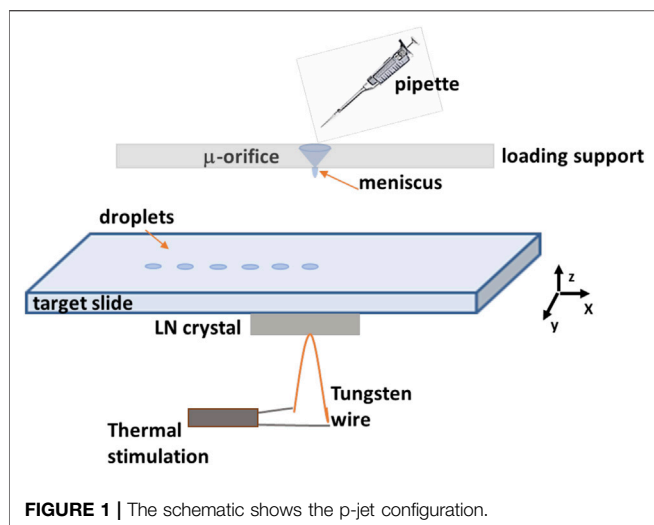
Zeta potential of the CTAB-coated nanoparticles was measured with a Malvern Zetasizer nano series (Malvern Instruments Ltd. Malvern, United Kingdom). For Z-potential measurements, a capillary cell type ZEN 1020 was employed. Zeta potential measurements were done before and after the centrifugation cycles to verify the AuNP solution stability. The reported value is the estimated mean of three measurements.

2.4.3 UV-VIS Spectroscopy

The optical properties of AuNPs and their molar concentration were measured by a UV spectrophotometer equipped with single monochromator (V-570 from Jasco, Easton, United States). Absorption spectra of the AuNP colloids were collected using a 1.00-cm quartz cell with a scan speed of 400 nm/min in the wavelength range from 300 to 800 nm. For the quantitative analysis of the gold amount in the AuNP solution, a set of six standards were obtained by diluting the as-prepared gold nanoparticle solution batch. Complete reduction from Au(III) to Au (0) was assumed.

2.4.4 Raman Spectroscopy

The SERS performance of AuNP colloids was evaluated by Raman spectroscopy using R6G as a molecular probe. The Raman and SERS spectra were collected by a confocal Raman spectrometer (Labspec Aramis, from Horiba-Jobin Yvon, Edison, NJ, United States) operating with a 632 nm diode laser as the exciting source. The 180° back-scattered radiation was collected by an Olympus metallurgical objective (MPlan $\times 10$, NA = 0.25) with confocal and slit apertures set to 400 μm ; a grating with



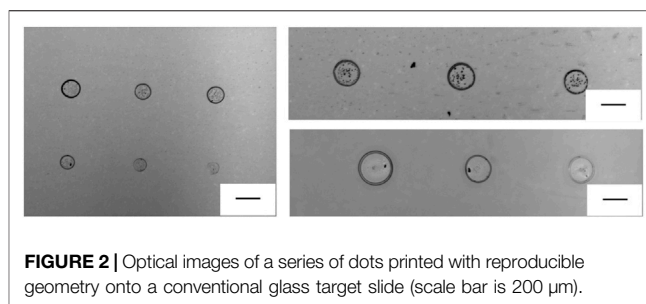
600 grooves/mm was used throughout. The radiation was focused onto a CCD detector (Synapse Mod. 354,308) cooled at -70°C by a Peltier module. The laser power measured at the output of the objective was 1.87 mW, which resulted in a power density of $1.9\text{ mW}/\mu\text{m}^2$. The reference spectrum of R6G was collected on a 2 mM aqueous solution with an exposure time of 8 s. The SERS spectrum of R6G was collected after AuNP functionalization with a 100 M ethanol solution of R6G (AuNPs/R6G, v/v 1:1) with an exposure time of 3 s. Both spectra were acquired by using a quartz cuvette with a chamber volume of 700 μl (Hellma GmbH and Co., Jena, Germany).

R6G was further used to test the SERS performance by running Raman imaging measurements in the mapping mode: the p-jet SERS substrate was placed on a piezo-electrically driven microscope stage with an x, y resolution of $10 \pm 0.5\text{ nm}$ and a \dot{a} resolution of $15 \pm 1\text{ nm}$. The stage was scanned at a constant speed in the x - y plane with an $8.0\text{-}\mu\text{m}$ step size. The spectra were collected by an Olympus metallurgical objective (MPlan $\times 10$, $\text{NA} = 0.25$) with a 632-nm diode laser, an exposure time of 10 s, and confocal and slit apertures set to 400 μm . The same acquisition parameters were used to carry out Raman imaging measurements on the substrate functionalized with BSA. The only difference was the step size that was settled to 5 μm . The reference BSA spectrum (bulk) was collected by an Olympus metallurgical objective (MPlan $\times 10$, $\text{NA} = 0.25$) with a 632-nm diode laser, an exposure time of 15 s, and confocal and slit apertures set to 400 μm . A 500- μM BSA water solution (120 μl) was dropped on an aluminum support and let dry at room temperature before the Raman acquisition. All the collected Raman data were converted into ASCII format and transferred to the MATLAB computational platform for further processing.

3 RESULTS AND DISCUSSION

3.1 Pyro-Electrohydrodynamic Jet System

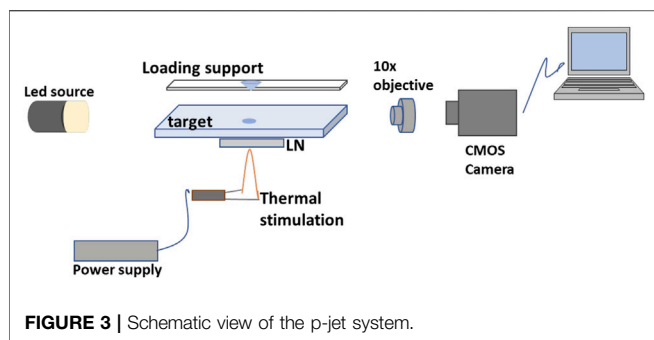
The basic principle of the p-jet printing is based on the pyroelectric effect and, therefore, on the use of ferroelectric



crystals (LN) and the manipulation of the liquid samples in the presence of an electric field generated pyroelectrically. **Figure 1** schematically shows the p-jet system, used here for fabricating the sensing surface. A mother drop of a solution sample containing an amount of gold nanoparticles is loaded directly in a micro-orifice of the loading support, allowing the formation of a thin liquid meniscus on the opposite side. Moreover, a standard XYZ micrometric manual translation stage is used for aligning the orifice with the central point of a piece of LN crystal, while a heating element made of tungsten wire is placed in contact with the crystal, and an electric field induced by the pyroelectric effect exerts an attractive force on the drop-meniscus deforming and generating liquid jet emission. The target slide, printing the tiny droplets, is inserted between the loading support with meniscus and the LN crystal.

The great advantage of this technique consists in the possibility of direct printing micro-drops onto a sensing surface, used as the receiving substrate. In fact, pyro-EHD printing allows to realize high-resolution samples, keeping good precision during the printing process, and fine spatial resolution onto a very large scale could be obtained. In addition, several nanostructured plasmonic sensor could be used through pyro-EHD printing. This technology has proven to be highly repeatable with spot diameter around 200 μm as shown in **Figure 2**. Moreover, the p-jet system has been improved with respect to the previously published study; these upgrades allowed us to improve the reproducibility of the micro-patterns in terms of size/geometry as shown in the next images.

Figure 3 shows a traditional optical path, consisting of a collimated LED, an optical microscope objective ($\times 10$), and a high-speed CMOS camera (Motion Pro Y3-S1, pixel size of $10.85\text{ }\mu\text{m}^2$), allowing us to observe the ejection event during the activation of the pyroelectric effect. The electric field generated by the pyroelectricity of the LN crystal causes the accumulation of charge on the free surface of the mother droplet through the electrostatic effect. The charge density is high enough to cause the well-known Coulomb repulsion effect (Collins et al., 2008; Gennari et al., 2015), which deforms the meniscus of the mother droplet into a so-called Taylor cone. When the electric field exceeds the surface tension of the liquid, tiny droplets are ejected from the apex of the meniscus (Hartman et al., 1999). The volume of sub-droplets produced by this p-jet system is in the range of 100 pL and are deposited on a simple microscope glass previously cleaned. After the first spot, we translate the deposition glass slide and generate a new



point of a colloidal solution containing gold nanoparticles under certain spatial constraints.

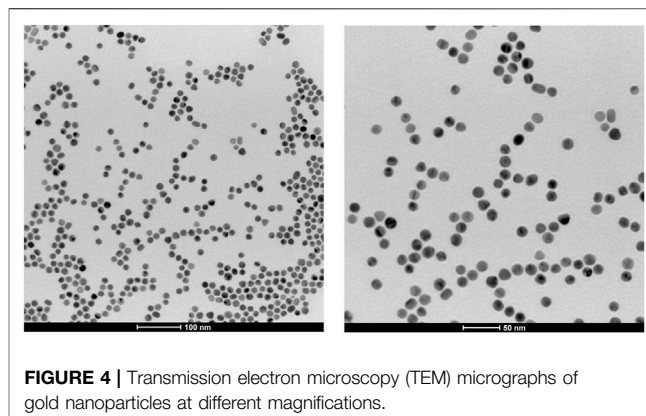
3.2 Colloid Characterization

According to our previous work (Pannico et al., 2018), the shape and shape distribution of the AuNPs were evaluated from SIA. Ten TEM images (nanoparticle population of about 900 units) were used for the analysis. In **Figure 4**, two representative TEM micrographs of the AuNPs are shown, at different magnifications: it was found that 98% of the population is characterized by a spherical shape ($R \geq 0.8$); it exhibits an average diameter of 16 ± 3 nm and a unimodal, Gaussian-like size distribution (cf **Supplementary Figure S1**). Only 2% of the total nanoparticle population was characterized by a rod-like shape ($R \leq 0.6$). In the whole set of TEM images, no particle aggregation was apparent. In fact, the CTAB surfactant adsorbs onto the AuNP metal surfaces forming a positively charged self-assembling bilayer (Suh and Moskovits, 1986) as confirmed by the zeta potential value of $+43 \pm 3$ mV. This value hardly changed, even after centrifugation and re-dispersion in Milli-Q water ($+40 \pm 2$ mV), confirming the stability of the bilayer structure (Nikoobakht and El-Sayed, 2001; Sau and Murphy, 2005; Das et al., 2008).

By UV-VIS measurements, the AuNP colloids exhibit a strong local surface plasmon resonance (LSPR) band around 526 nm with a narrow shape, which, in accordance with the SIA results, is indicative of a unimodal distribution of particle sizes (see **Supplementary Figure S1**, **Supplementary Material S1**). The Au molar concentration in the colloidal solution was evaluated by using a calibration curve. The Au molar concentration was estimated to be 2 mM. According to our previous work (Pannico et al., 2018), by coupling the TEM geometrical parameters (size and shape) and the UV-VIS results [(Au)], the concentration of the colloid solution in terms of nanospheres was estimated to be 17 nM. This AuNP batch was used for the fabrication of the p-jet SERS substrate. The SERS performance of the synthesized AuNPs was evaluated in terms of absolute enhancement factor (EF). The EF was estimated by comparing the spontaneous and the SERS spectra of R6G:

$$EF = (I_{\text{SERS}} \times N_{\text{REF}}) / (I_{\text{REF}} \times N_{\text{SERS}})$$

where I_{SERS} is the integrated area of a specific SERS signal (at $1,510 \text{ cm}^{-1}$) and I_{REF} is the integrated area of the corresponding Raman signal (at $1,519 \text{ cm}^{-1}$), both normalized for the exposure



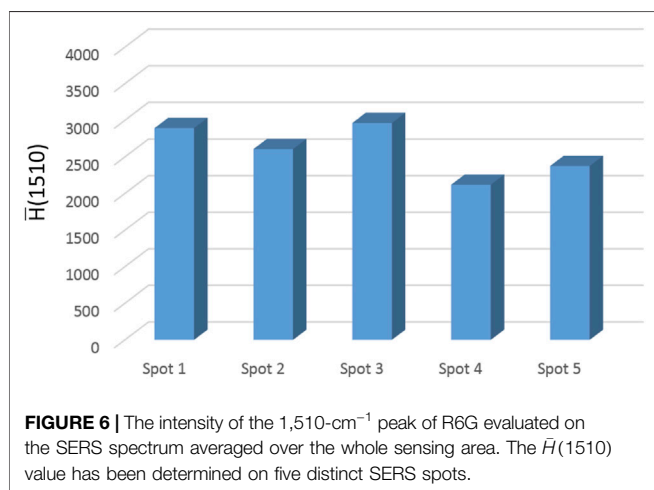
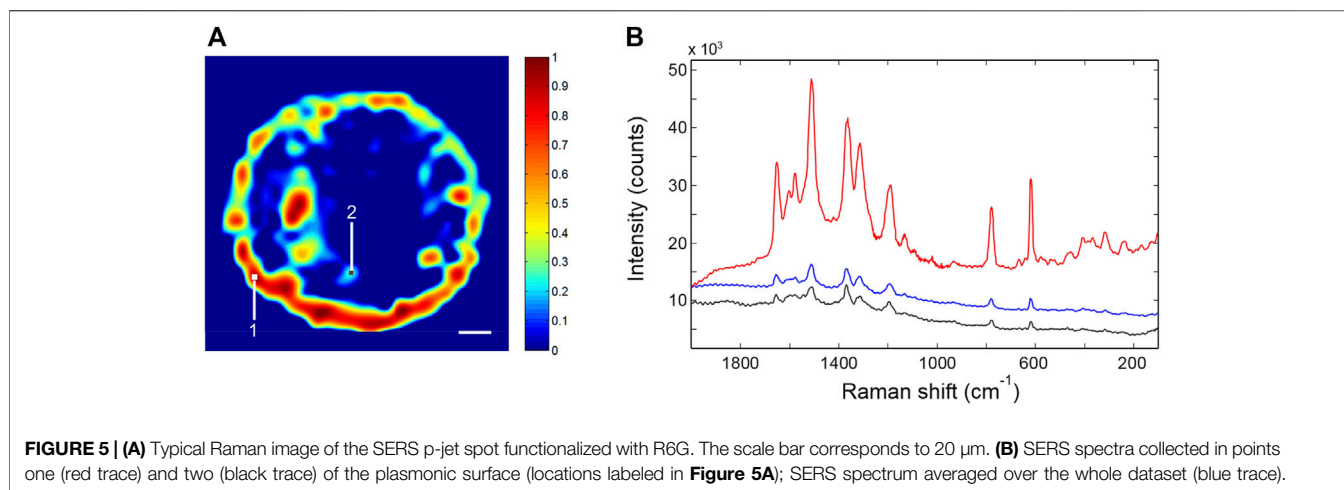
time. Analogously, N_{SERS} and N_{REF} represent the number of molecules contributing to the SERS and the Raman signal, respectively. More details on the EF calculation are reported in our previous work (Sjöberg et al., 2014). The EF value of the AuNP colloid was 2.5×10^5 , a figure suitable for hypersensitive analytical applications.

3.3 SERS Response With R6G

The SERS activity was investigated by Raman imaging experiments. The first analysis was performed by use of R6G as molecular reporter, owing to its exceptional inelastic scattering and the well-characterized adsorbate structure (Qiu et al., 2006; Le Ru et al., 2007). After R6G surface functionalization, an area of $200 \times 200 \mu\text{m}$ was mapped with a spatial resolution of $8.0 \mu\text{m}$. Five spots were mapped, and a representative Raman image, reconstructed by considering the intensity of the R6G peak at $1,510 \text{ cm}^{-1}$, is reported in **Figure 5A**. The SERS spectrum averaged over the whole dataset and two spectra collected in different points of the sensing area (labeled one and two in the Raman image) are compared in **Figure 5B**.

The SERS activity is strong, albeit the signal distribution is not fully homogeneous. The intensity is larger around the spot boundary (a coffee-ring effect), but regions of intense signaling are also found inside the active surface. The R6G spectrum is highly reproducible. The intensity of the $1,510 \text{ cm}^{-1}$ peak, averaged over the whole sensing area, is represented in **Figure 6** for the five analyzed SERS spots. It is found that the adopted fabrication method consistently affords the confinement of the nanoparticle assembly in a round-shaped disc having a size in the range $100\text{--}150 \mu\text{m}$; this nanostructured pattern displays a well-detectable and reproducible SERS response [$\bar{H}(1510) = 2592 \pm 353$].

The distribution of the nanospheres within the sensing area can be made more homogeneous to alleviate under sampling issues. A promising approach to achieve this result, actively investigated in our laboratories, is the derivatization of the substrate surface. The enhancement factor of this SERS substrate was evaluated by comparing the Raman and SERS spectra of R6G. The reference Raman spectrum was collected in the solution. The number of scattering molecules in the sampling volume was estimated to be 2.73×10^9 . We used the



integrated peak area at $1,510$ and $1,519\text{ cm}^{-1}$ for SERS and Raman, respectively. The EF was evaluated in the region of the highest SERS activity (red trace in **Figure 5B**), due to the inhomogeneous distribution of the nanoparticles in the sensing area, which prevents a reliable averaging of the surface coverage; it amounts to 3.0×10^4 . More details on the EF calculations are reported in the Supplementary Material. The EF of the SERS substrate is lower than that measured on the colloidal solution, which is representative of the intrinsic nanoparticle activity. In our opinion, the effect can be ascribed to the incomplete coverage of the plasmonic surface due to a transfer/rinsing protocol yet to be optimized. **Table 2** shows the results obtained for the five p-jet spots in terms of size and SERS activity. In both cases, a coefficient of variation much below than 15% was achieved.

TABLE 2 | Measurement results for the five p-jet spot: mean spots diameter, average SERS intensity, and coefficient of variation values.

Parameter	Mean (\pm SD)	Coefficient of variation (CV)
Diameter (μm)	109 (\pm 8)	7
Intensity (a.u.)	2,592 (\pm 353)	13

The results clearly show the high level of reproducibility both in terms of spot diameter, with a coefficient of variation less than 10%, and in terms of SERS response with a coefficient of variation less than 15%. Therefore, the step forward in the p-jet configuration presented in this work is of fundamental importance for increasing the statistical validity of the innovative p-jet SERS substrate. Compared to Pannico et al. (2020), where we demonstrated for the first time the proof of concept of a completely new p-jet SERS substrate, here we refine the p-jet configuration demonstrating the statistical validity of the technique, thanks to the high reproducibility reported in **Table 2**, a fundamental aspect for any analytical application.

3.4 SERS Response With BSA

The p-jet SERS substrate is characterized here for the first time in case of a typical test protein, the BSA, considering that SERS spectroscopy is a highly promising approach for biosensing (Westermeier and Marouga, 2005; Han et al., 2009; Kuhar et al., 2021). **Figures 7A,B** show two typical Raman images obtained for the SERS p-jet spots in which a $100\text{-}\mu\text{M}$ solution of BSA was drop-casted. The SERS spectrum collected at a point of maximum activity is shown in **Figure 7C**, red trace. Image reconstruction was performed by representing the intensity of the peak at 216 cm^{-1} as a function of the collection coordinates. As

TABLE 1 | Electrical and thermal characteristics of the heater.

Heater	R (Ω)	I_{ON} (A)	ON time (s)	OFF time (s)	P_{ON} (W)	P_{MEAN} (W)	T_{ON} ($^{\circ}\text{C}$)
Tungsten wire	0.2	8.5	3.5	56.5	14.5	0.85	120

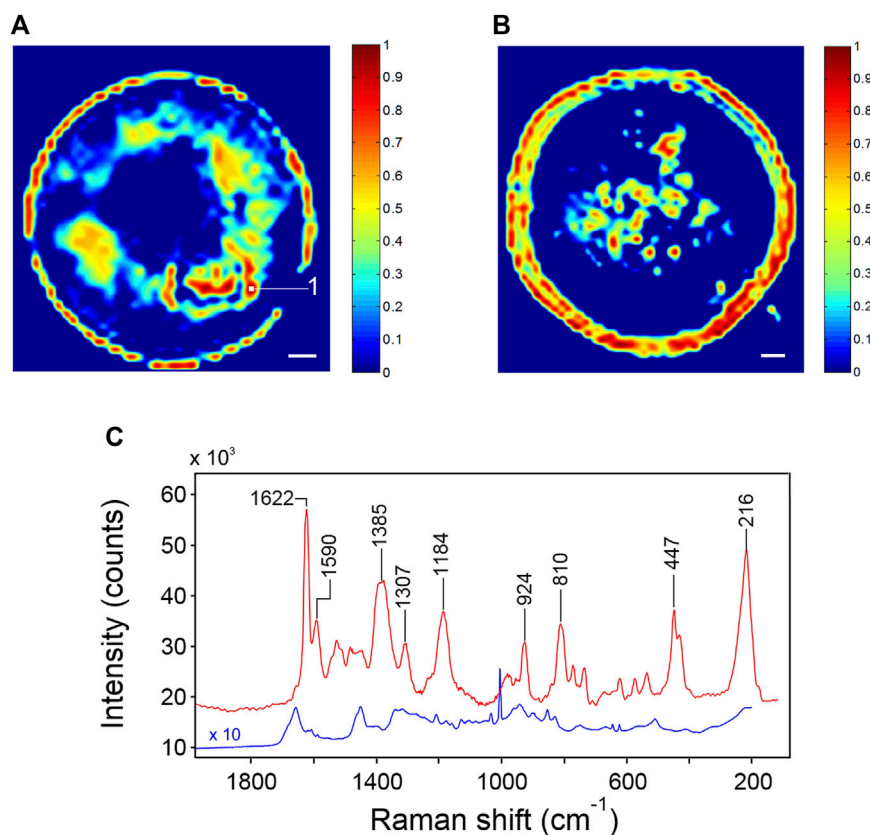


FIGURE 7 | (A,B) Raman images of two representative SERS spots functionalized with a 100- μM solution of BSA. The image reconstruction was made by considering the intensity of the 216- cm^{-1} peak. The scale bar is 20 μm . **(C)** SERS spectrum of BSA collected in point one of **Figure 7A** (red trace); Raman spectrum of solid BSA (blue trace).

for the case of R6G, SERS activity is larger in the periphery of the deposition but, especially in the map of **Figure 7A**, regions of intense signaling are present in the whole area. The round shape of the spots is well defined, confirming the efficiency of the p-jet for the nanostructure confinement. The SERS spectrum of BSA in the areas of high throughput is intense in comparison to previously reported spectra (Das et al., 2009; Iosin et al., 2009; Szekeres and Kneipp, 2018), which denotes a remarkable sensitivity of the proposed platform. The highest EF amounts to 6.6×10^5 ; the value averaged on the whole sensing area and on five different spots is 2.5×10^4 . Also in this case, the platform sensitivity could be further exploited by making the nanoparticle distribution more homogeneous.

In **Figure 7C**, the SERS spectrum of BSA collected on the present plasmonic platform (red trace) is compared with the Raman spectrum of BSA in the solid state (blue trace). BSA is a weak Raman scatterer: in the solution, the Raman spectrum is barely detectable (Kuhar et al., 2021), but in the dehydrated form, it can be collected with a good SNR and an adequate resolution. The spectrum is reported in full in **Supplementary Figure S3**, Supplementary Material. As expected, the pattern is complex, reflecting the composition of the protein (583 amino acids, with the aromatic residues accounting for 8.2% of the total). Despite the reduced content, aromatics display numerous signals (e.g., at

1,032, 852, 828, 643, and 622 cm^{-1} , among others) in the form of characteristically sharp peaks, owing to the large Raman cross-section of the relatively normal modes. The prominent signal at 1,003 cm^{-1} is due to a breathing mode of the phenyl ring. Broader bands, usually displaying multicomponent structures (e.g., at 1,655, 1,268, and 941 cm^{-1}), originate from the amide linkage and reflect its conformational and H-bonding sensitivity. Methylene groups give rise to an intense signal at 1,449 cm^{-1} .

The SERS spectrum of BSA deposited on the nanosphere assembly differs substantially from its Raman counterpart. As a preliminary observation, it is noted that the SERS pattern is simpler and considerably more resolved. This effect is likely due to the existence of a preferential interaction site within the protein structure, so that the observed pattern is only representative of the amino acid residue(s) in direct contact with the metal surface. In the SERS spectrum, the main peak occurs at 1,622 cm^{-1} : its sharpness, symmetry, and intensity are indicative of a specific functional group in direct contact with the gold surface. BSA displays both negatively charged domains [glutamic or aspartic acid (Glu/Asp), which, at neutral pH, occur in the glutamate/aspartate form] and positively charged domains (lysine or histidine). The nanospheres of the present platform display a positive surface charge ($+43 \pm 3$ mV, as per z -potential measurements), suggesting an interaction mechanism through

carboxylate ions. In fact, the $1,622\text{ cm}^{-1}$ component has been associated to the antisymmetric stretching of the $-\text{COO}^-$ group (Aliaga et al., 2009; Chuang and Chen, 2009). The close proximity of the carboxylate anion to the metal surface is confirmed by the substantial intensity of other signals originating from this functional group, at $1,385\text{ cm}^{-1}$ (the COO^- symmetric stretching) at 924 cm^{-1} (the $\text{C}-\text{COO}^-$ stretching), and at $447/430\text{ cm}^{-1}$ (out-of-plane deformation modes) (Aliaga et al., 2009).

The well-resolved peak at $1,590\text{ cm}^{-1}$ has been also related to the $\nu_{\text{as}}(\text{COO}^-)$ mode (Sjöberg et al., 2014) and is tentatively ascribed to the occurrence of an alternative adsorbate conformation. An important band at $1,184\text{ cm}^{-1}$ remains to be elucidated. The intense signal at 216 cm^{-1} , entirely absent in the Raman spectrum, has been already reported at close frequencies for a series of amino acids adsorbed on silver colloids (Suh and Moskovits, 1986). It was ascribed to a generic “metal–molecule vibration,” in the present case a COO^- Au deformation. This band is important for several reasons: it is the second most intense feature of the SERS spectrum and is fully resolved, which makes it an ideal candidate for analytical purposes and imaging reconstruction. It is a direct signature of the analyte-to-metal interaction and, upon a complete vibrational characterization, may provide relevant information on the adsorbate structure. A further notable observation is the absence of aromatic signals in the SERS spectrum (in particular, the lack of the intense peak at $1,004\text{ cm}^{-1}$) and the reduced intensity of the methylene deformation band. This confirms the two non-aromatic residues Glu and Asp as the most likely binding sites and suggests that the carboxylate ion is oriented in such a way to displace the methylene group from the metal surface.

The SERS spectrum of BSA across all the sensing surfaces was remarkably reproducible. This observation, which has relevant implications in biosensing, was quantitatively verified by applying multivariate analysis to the hyperspectral datasets. A principal component analysis (PCA) reduces in a compact form the information broadly distributed in large spectral data; it yields two matrices called scores and loadings that, taken together, reproduce the data variance (Malinowski, 1991). One of the aims of the analysis is to identify the minimum number of linearly independent components (principal components, PC) that is necessary to simulate the dataset. When applied to hyperspectral measurements taken on a mixture, this figure represents the number of individual components contributing to the overall pattern (Martens and Næs, 1989; Windig et al., 2005).

PCA applied to the hyperspectral data of **Figure 7A** (details of the analysis are reported in **Supplementary Figures S4, 5**) yielded two significant PCs (PC1 and PC2) accounting for 99.54% of the total variance. Of these, PC1 accounts for 99.17% and PC2 for 0.43% of the total variance. The remaining 0.4% was due to random noise. In practice, a single spectrum (PC1) is able to reproduce the whole dataset composed of 1,935 spectra. Essentially coincident results were obtained for the remaining four spots. This finding is in contrast with those reported in Szekeres and Kneipp (2018) on the SERS response of the protein corona of gold nanoparticles. The spectra collected on colloidal solutions were weak, complex, and displayed large point-to-point variability. These results were interpreted assuming that BSA is unable to substitute the stabilizing citrate layer surrounding the nanoparticles, and the binding occurs *via* electrostatic interaction of the lysine residues with the citrate layer. The complex and poorly

resolved SERS patterns were ascribed to an enhanced conformational flexibility of the protein binding sites. A similar behavior was observed for L-lysine adsorbed on silver colloids (Aliaga et al., 2009). In our case, the nanospheres are surrounded by a CTAB bilayer, which is easier to displace than the citrate monolayer (Hunter, 1989; Pannico and Musto, 2021). The consistency of the SERS spectrum, demonstrated by PC analysis, suggests a highly specific orientation/conformational arrangement of the adsorbate, which implies a direct contact of the binding site with the gold surface as a consequence of the bilayer displacement. The reproducible SERS pattern of BSA is the first fundamental step in the direction of future bioanalytical applications.

4 CONCLUSION

In the present contribution, we describe the fabrication of spatially confined SERS surfaces having precisely controlled shape and size, by means of an advanced ink-jet printing technique called pyro-electrohydrodynamic jet printing. This methodology affords the realization of reproducible nanoparticle assemblies with a round shape and a diameter in the 100–200- μm range. This SERS substrate has been developed to optimize single-measurement sampling with current micro-Raman instrumentation. In fact, they improve the platform sensitivity by concentrating the nanospheres in a micro-sized surface and minimize under sampling issues. The SERS activity, tested with R6G was found to be strong and reproducible for a series of five consecutive constructs. Further improvement in the nanoparticle distribution within the sensing area is expected by surface derivatization. The SERS response was also tested for a typical test protein, the BSA, by drop-casting a 100- μM solution of BSA after p-jet spotting. Intense SERS activity was revealed across the whole surface. Furthermore, spectra collected in different locations displayed excellent consistency, as demonstrated by multivariate analysis of the imaging hyperspectral data. The characterization results presented in this work represent the first demonstration of the robustness of this kind of SERS substrate and open the route to future tests for biosensing applications.

DATA AVAILABILITY STATEMENT

The original contributions presented in the study are included in the article/**Supplementary Material**, further inquiries can be directed to the corresponding authors.

AUTHOR CONTRIBUTIONS

PF, PM, and SG conceived and designed the research, VV, MP, and RR performed the experiments and took care of the sample preparation, HO and YN have engineered micro-orifice of the loading support. All the authors wrote the manuscript and revised the results.

ACKNOWLEDGMENTS

The authors acknowledge the EU funding within the Horizon 2020 Program, under the FETOPEN Project “SensApp,” Grant Agreement n.829104.

REFERENCES

- Aliaga, A. E., Osorio-Roman, I., Garrido, C., Leyton, P., Cárcamo, J., Clavijo, E., et al. (2009). Surface Enhanced Raman Scattering Study of L-Lysine. *Vibrational Spectrosc.* 50, 131–135. doi:10.1016/j.vibspec.2008.09.018
- Aroca, R. (2006). *Surface-enhanced Vibrational Spectroscopy*. England: John Wiley & Sons.
- Bergveld, P. (1991). A Critical Evaluation of Direct Electrical Protein Detection Methods. *Biosens. Bioelectron.* 6, 55–72. doi:10.1016/0956-5663(91)85009-1
- Chuang, C.-H., and Chen, Y.-T. (2009). Raman Scattering of L-tryptophan Enhanced by Surface Plasmon of Silver Nanoparticles: Vibrational Assignment and Structural Determination. *J. Raman Spectrosc.* 40, 150–156. doi:10.1002/jrs.2097
- Collins, R. T., Jones, J. J., Harris, M. T., and Basaran, O. A. (2008). Electrohydrodynamic Tip Streaming and Emission of Charged Drops from Liquid Cones. *Nat. Phys.* 4, 149–154. doi:10.1038/nphys807
- Das, G., Mecarini, F., Gentile, F., De Angelis, F., Mohan Kumar, H., Candeloro, P., et al. (2009). Nano-patterned SERS Substrate: Application for Protein Analysis vs. Temperature. *Biosens. Bioelectron.* 24, 1693–1699. doi:10.1016/j.bios.2008.08.050
- Das, M., Mordoukhovski, L., and Kumacheva, E. (2008). Sequestering Gold Nanorods by Polymer Microgels. *Adv. Mater.* 20, 2371–2375. doi:10.1002/adma.200702860
- Domon, B., and Aebersold, R. (2006). Mass Spectrometry and Protein Analysis. *Science* 312, 212–217. doi:10.1126/science.1124619
- Ferraro, P., Coppola, S., Grilli, S., Paturzo, M., and Vespini, V. (2010). Dispensing Nano-Pico Droplets and Liquid Patterning by Pyroelectrodynamic Shooting. *Nat. Nanotech* 5, 429–435. doi:10.1038/nnano.2010.82
- Fornasaro, S., Alsamad, F., Baia, M., Batista de Carvalho, L. A. E., Beleites, C., Byrne, H. J., et al. (2020). Surface Enhanced Raman Spectroscopy for Quantitative Analysis: Results of a Large-Scale European Multi-Instrument Interlaboratory Study. *Anal. Chem.* 92, 4053–4064. doi:10.1021/acs.analchem.9b05658
- Foti, A., D’Andrea, C., Villari, V., Micali, N., Donato, M., Fazio, B., et al. (2018). Optical Aggregation of Gold Nanoparticles for SERS Detection of Proteins and Toxins in Liquid Environment: Towards Ultrasensitive and Selective Detection. *Materials* 11, 440. doi:10.3390/ma11030440
- García-Lojo, D., Núñez-Sánchez, S., Gómez-Graña, S., Grzelczak, M., Pastoriza-Santos, I., Pérez-Juste, J., et al. (2019). *Plasmonic Supercrystals*. *Acc. Chem Res* 52, 1855–1864.
- Gennari, O., Battista, L., Silva, B., Grilli, S., Miccio, L., Vespini, V., et al. (2015). Investigation on Cone Jetting Regimes of Liquid Droplets Subjected to Pyroelectric fields Induced by Laser Blasts. *Appl. Phys. Lett.* 106, 054103. doi:10.1063/1.4907005
- Han, X. X., Jia, H. Y., Wang, Y. F., Lu, Z. C., Wang, C. X., Xu, W. Q., et al. (2008). Analytical Technique for Label-free Multi-Protein Detection Based on Western Blot and Surface-Enhanced Raman Scattering. *Anal. Chem.* 80, 2799–2804. doi:10.1021/ac702390u
- Han, X. X., Zhao, B., and Ozaki, Y. (2009). Surface-enhanced Raman Scattering for Protein Detection. *Anal. Bioanal. Chem.* 394, 1719–1727. doi:10.1007/s00216-009-2702-3
- Hartman, R. P. A., Brunner, D. J., Camelot, D. M. A., Marijnissen, J. C. M., and Scarlett, B. (1999). Electrohydrodynamic Atomization in the Cone-Jet Mode Physical Modeling of the Liquid Cone and Jet. *J. Aerosol Sci.* 30, 823–849. doi:10.1016/s0021-8502(99)00033-6
- Hillger, F., Nettels, D., Dorsch, S., and Schuler, B. (2007). Detection and Analysis of Protein Aggregation with Confocal Single Molecule Fluorescence Spectroscopy. *J. Fluoresc* 17, 759–765. doi:10.1007/s10895-007-0187-z
- Hunter, R. J. (1989). *Foundations of Colloid Science*. Oxford, UK: Clarendon Press.

SUPPLEMENTARY MATERIAL

The Supplementary Material for this article can be found online at: <https://www.frontiersin.org/articles/10.3389/fbioe.2022.817736/full#supplementary-material>

- Iosin, M., Toderas, F., Baldeck, P. L., and Astilean, S. (2009). Study of Protein-Gold Nanoparticle Conjugates by Fluorescence and Surface-Enhanced Raman Scattering. *J. Mol. Struct.* 924–926, 196–200. doi:10.1016/j.molstruc.2009.02.004
- Kuhar, N., Sil, S., and Umapathy, S. (2021). Potential of Raman Spectroscopic Techniques to Study Proteins. *Spectrochimica Acta A: Mol. Biomol. Spectrosc.* 258. doi:10.1016/j.saa.2021.119712
- Ladokhin, A. S. (2006). “Fluorescence Spectroscopy in Peptide and Protein Analysis,” in *Encyclopedia of Analytical Chemistry*.
- Le Ru, E. C., Blackie, E., Meyer, M., and Etchegoin, P. G. (2007). Surface Enhanced Raman Scattering Enhancement Factors: a Comprehensive Study. *J. Phys. Chem. C* 111, 13794–13803. doi:10.1021/jp0687908
- Le Ru, E., and Etchegoin, P. (2008). *Principles of Surface-Enhanced Raman Spectroscopy: And Related Plasmonic Effects*. Oxford, UK: Elsevier.
- Lee, H.-H., Chou, K.-S., and Huang, K.-C. (2005). Inkjet Printing of Nanosized Silver Colloids. *Nanotechnology* 16, 2436–2441. doi:10.1088/0957-4484/16/10/074
- Lee, T., Kwon, S., Jung, S., Lim, H., and Lee, J.-J. (2019). Macroscopic Ag Nanostructure Array Patterns with High-Density Hotspots for Reliable and Ultra-sensitive SERS Substrates. *Nano Res.* 12, 2554–2558. doi:10.1007/s12274-019-2484-7
- Lin, S., Lin, X., Shang, Y., Han, S., Hasi, W., and Wang, L. (2019). Self-Assembly of Faceted Gold Nanocrystals for Surface-Enhanced Raman Scattering Application. *J. Phys. Chem. C* 123, 24714–24722. doi:10.1021/acs.jpcc.9b06686
- Malinowski, E. R. (1991). *Factor Analysis in Chemistry*. New York: John Wiley & Sons.
- Mann, M., Hendrickson, R. C., and Pandey, A. (2001). Analysis of Proteins and Proteomes by Mass Spectrometry. *Annu. Rev. Biochem.* 70, 437–473. doi:10.1146/annurev.biochem.70.1.437
- Martens, H., and Naes, T. (1989). *Multivariate Calibration*. Chichester: John Wiley & Sons.
- McGovern, C. M., Rades, T., and Gordon, K. C. (2008). Recent Pharmaceutical Applications of Raman and Terahertz Spectroscopies. *J. Pharm. Sci.* 97, 4598–4621. doi:10.1002/jps.21340
- Nie, Z., and Kumacheva, E. (2008). Patterning Surfaces with Functional Polymers. *Nat. Mater* 7, 277–290. doi:10.1038/nmat2109
- Nikobakht, B., and El-Sayed, M. A. (2001). Evidence for Bilayer Assembly of Cationic Surfactants on the Surface of Gold Nanorods. *Langmuir* 17, 6368–6374. doi:10.1021/la010530o
- Pannico, M., Calarco, A., Peluso, G., and Musto, P. (2018). Functionalized Gold Nanoparticles as Biosensors for Monitoring Cellular Uptake and Localization in normal and Tumor Prostatic Cells. *Biosensors* 8, 87. doi:10.3390/bios8040087
- Pannico, M., Musto, P., Rega, R., Vespini, V., Grilli, S., and Ferraro, P. (2020). Direct Printing of Gold Nanospheres from Colloidal Solutions by Pyro-Electrohydrodynamic Jet Allows Hypersensitive SERS Sensing. *Appl. Surf. Sci.* 531, 147393. doi:10.1016/j.apsusc.2020.147393
- Pannico, M., and Musto, P. (2021). SERS Spectroscopy for the Therapeutic Drug Monitoring of the Anticancer Drug 6-Mercaptopurine: Molecular and Kinetic Studies. *Appl. Surf. Sci.* 539, 148225. doi:10.1016/j.apsusc.2020.148225
- Qiu, T., Wu, X. L., Shen, J. C., and Chu, P. K. (2006). Silver Nanocrystal Superlattice Coating for Molecular Sensing by Surface-Enhanced Raman Spectroscopy. *Appl. Phys. Lett.* 89, 131914. doi:10.1063/1.2357548
- Sau, T. K., and Murphy, C. J. (2005). Self-assembly Patterns Formed upon Solvent Evaporation of Aqueous Cetyltrimethylammonium Bromide-Coated Gold Nanoparticles of Various Shapes. *Langmuir* 21, 2923–2929. doi:10.1021/la047488s
- Schlucker, S. (2011). *Analytical, Biophysical and Life Science Applications*. Weinheim, Germany: WILEY-VCH Verlag & Co. Surface Enhanced Raman Spectroscopy

- Shin, K., and Chung, H. (2013). Wide Area Coverage Raman Spectroscopy for Reliable Quantitative Analysis and its Applications. *Analyst* 138, 3335–3346. doi:10.1039/c3an36843b
- Sjöberg, B., Foley, S., Cardey, B., and Enescu, M. (2014). An Experimental and Theoretical Study of the Amino Acid Side Chain Raman Bands in Proteins. *Spectrochimica Acta Part A: Mol. Biomol. Spectrosc.* 128, 300–311.
- Strachan, C. J., Rades, T., Gordon, K. C., and Rantanen, J. (2010). Raman Spectroscopy for Quantitative Analysis of Pharmaceutical Solids. *J. Pharm. Pharmacol.* 59, 179–192. doi:10.1211/jpp.59.2.0005
- Suh, J. S., and Moskovits, M. (1986). Surface-enhanced Raman Spectroscopy of Amino Acids and Nucleotide Bases Adsorbed on Silver. *J. Am. Chem. Soc.* 108, 4711–4718. doi:10.1021/ja00276a005
- Szekeres, G. P., and Kneipp, J. (2018). Different Binding Sites of Serum Albumins in the Protein corona of Gold Nanoparticles. *Analyst* 143, 6061–6068. doi:10.1039/c8an01321g
- Wang, A., and Kong, X. (2015). Review of Recent Progress of Plasmonic Materials and Nano-Structures for Surface-Enhanced Raman Scattering. *Materials* 8, 3024–3052. doi:10.3390/ma8063024
- Westermeier, R., and Marouga, R. (2005). Protein Detection Methods in Proteomics Research. *Biosci. Rep.* 25, 19–32. doi:10.1007/s10540-005-2845-1
- Windig, W., Gallagher, N. B., Shaver, J. M., and Wise, B. M. (2005). A New Approach for Interactive Self-Modeling Mixture Analysis. *Chemometrics Intell. Lab. Syst.* 77, 85–96. doi:10.1016/j.chemolab.2004.06.009
- Yakovlev, A. V., Milichko, V. A., Vinogradov, V. V., and Vinogradov, A. V. (2016). Inkjet Color Printing by Interference Nanostructures. *ACS Nano* 10, 3078–3086. doi:10.1021/acsnano.5b06074
- Yang, Q., Deng, M., Li, H., Li, M., Zhang, C., Shen, W., et al. (2015). Highly Reproducible SERS Arrays Directly Written by Inkjet Printing. *Nanoscale* 7, 421–425. doi:10.1039/c4nr04656k
- Yu, W. W., and White, I. M. (2010). Inkjet Printed Surface Enhanced Raman Spectroscopy Array on Cellulose Paper. *Anal. Chem.* 82, 9626–9630. doi:10.1021/ac102475k
- Zhang, C.-L., Lv, K.-P., Cong, H.-P., and Yu, S.-H. (2012). Controlled Assemblies of Gold Nanorods in PVA Nanofiber Matrix as Flexible Free-Standing SERS Substrates by Electrospinning. *Small* 8, 648–653. doi:10.1002/smll.201102230

Conflict of Interest: The authors declare that the research was conducted in the absence of any commercial or financial relationships that could be construed as a potential conflict of interest.

Publisher's Note: All claims expressed in this article are solely those of the authors and do not necessarily represent those of their affiliated organizations, or those of the publisher, the editors and the reviewers. Any product that may be evaluated in this article, or claim that may be made by its manufacturer, is not guaranteed or endorsed by the publisher.

Copyright © 2022 Vespini, Grilli, Ferraro, Rega, Ottevaere, Nie, Musto and Pannico. This is an open-access article distributed under the terms of the Creative Commons Attribution License (CC BY). The use, distribution or reproduction in other forums is permitted, provided the original author(s) and the copyright owner(s) are credited and that the original publication in this journal is cited, in accordance with accepted academic practice. No use, distribution or reproduction is permitted which does not comply with these terms.